

The relevance of ambipolar diffusion for neutron star evolution

Andrea Passamonti^{1,2*}, Taner Akgün¹, José A. Pons¹, Juan A. Miralles¹

¹*Department de Física Aplicada, Universitat d'Alacant, Ap. Correus 99, 03080 Alacant, Spain*

²*INAF-Osservatorio Astronomico di Roma, via Frascati 44, I-00040, Monteporzio Catone (Roma), Italy*

3 October 2018

ABSTRACT

We study ambipolar diffusion in strongly magnetised neutron stars, with special focus on the effects of neutrino reaction rates and the impact of a superfluid/superconducting transition in the neutron star core. For axisymmetric magnetic field configurations, we determine the deviation from β -equilibrium induced by the magnetic force and calculate the velocity of the slow, quasi-stationary, ambipolar drift. We study the temperature dependence of the velocity pattern and clearly identify the transition to a predominantly solenoidal flow. For stars without superconducting/superfluid constituents and with a mixed poloidal-toroidal magnetic field of typical magnetar strength, we find that ambipolar diffusion proceeds fast enough to have a significant impact on the magnetic field evolution only at low core temperatures, $T \lesssim 1 - 2 \times 10^8$ K. The ambipolar diffusion timescale becomes appreciably shorter when fast neutrino reactions are present, because the possibility to balance part of the magnetic force with pressure gradients is reduced. We also find short ambipolar diffusion timescales in the case of superconducting cores for $T \lesssim 10^9$ K, due to the reduced interaction between protons and neutrons. In the most favourable scenario, with fast neutrino reactions and superconducting cores, ambipolar diffusion results in advection velocities of several km/kyr. This velocity can substantially reorganize magnetic fields in magnetar cores, in a way that can only be confirmed by dynamical simulations.

Key words: methods: numerical – stars: evolution – stars: magnetars – stars: magnetic field – stars: neutron.

1 INTRODUCTION

The understanding of long term evolution of magnetic fields in neutron stars (NSs) is crucial to connect possible evolutionary tracks between NS classes. The origin, structure and dynamics of the large-scale magnetic fields in magnetars and high-B pulsars, and their influence on observable emission processes have been the subject of many studies. The answers to these (strongly interrelated) issues must explain why the magnetic field strength, inferred from astrophysical observations, can vary by many orders of magnitude, from recycled millisecond pulsars with dipolar magnetic fields of about $10^8 - 10^9$ G, to “normal” rotation powered pulsars with fields between 10^{10} and 10^{13} G, and super-strong fields of magnetars, up to 10^{15} G. Besides their persistent emission, magnetars show frequent outbursts and flares, which can release up to 10^{46} erg s⁻¹ (for more details see e.g. Mereghetti 2008; Mereghetti et al. 2015; Turolla et al. 2015). This rich phenomenology is usually attributed to lo-

cally stronger fields (higher order multipoles, coronal loops, strong crustal toroidal fields). Being isolated and slowly rotating stars, neither accretion nor rotation can supply the required energy. It is therefore important to understand the details of the internal evolution of magnetic fields, and their links to the magnetosphere and observable effects.

The internal magnetic field of a neutron star evolves mainly through three processes: Ohmic diffusion, Hall drift and ambipolar diffusion (Goldreich & Reisenegger 1992; Shalybkov & Urpin 1995). The combined effect of Ohmic decay and Hall drift is dominant in the crust. Special attention has been paid to the key role of the Hall drift in the crust of NSs, with plenty of studies over the last decades (Hollerbach & Rüdiger 2002, 2004; Pons & Geppert 2007; Reisenegger et al. 2007; Pons et al. 2009; Kondić et al. 2011; Viganò et al. 2012; Gourgouliatos et al. 2013; Marchant et al. 2014; Gourgouliatos & Cumming 2014, 2015; Gourgouliatos et al. 2015). Among all, Viganò et al. (2013) performed the most complete study of the magnetic and thermal evolution of isolated NSs, exploring the influence of their initial magnetic field strength and geometry, their mass, envelope com-

* E-mail: passamonti@ua.es

position and relevant microphysical parameters. Using the same numerical code, Pons, Viganò & Rea (2013) showed that a highly resistive layer in the deep crust is a crucial ingredient for enhancing dissipation of magnetic energy of high-field NSs. The majority of these works present 2D simulations, but recent 3D simulations suggest that the Hall-induced small scale magnetic features persist in the NS crust on longer time scales than in axisymmetric 2D simulations, although the global evolution still tends to the dipolar Hall attractor (Wood & Hollerbach 2015).

Concerning possible mechanisms operating in magnetar cores, the number of works is sensibly smaller, and with far less detail than for the crustal field evolution. Owing to its quadratic dependence on the magnetic field strength, ambipolar diffusion was proposed (Goldreich & Reisenegger 1992) as the main process controlling the evolution of magnetars during the first $10^3 - 10^5$ yr. However, a neutron star core cools down below the neutron-superfluid and proton-superconducting critical temperatures very fast, and the interaction between the various particle species and the magnetic field becomes much more complex than in the standard MHD approach. Nevertheless, Goldreich & Reisenegger (1992) argued that ambipolar diffusion would still be a significant process in these cases. On the other hand, Glampedakis et al. (2011b) studied in more detail the ambipolar diffusion in superfluid and superconducting stars, and concluded that its role on the magnetic field evolution would be negligible. This is one of the issues that we address in this paper. Other recent works (Graber et al. 2015; Elfriz et al. 2016) have also shown that, without considering ambipolar diffusion, the magnetic flux expulsion from the NS core with superconducting protons is very slow.

The effect of ambipolar diffusion has been so far studied through simple timescale estimates, with sparse isolated attempts to engage simulations in a simplified 1D approach (Hoyos et al. 2008, 2010). In this work, we revisit this important topic in a more detailed way, including realistic microphysics inputs, with the purpose of setting up the stage for multidimensional numerical simulations. We aim at improving previous estimates by calculating global velocity fields (as opposed to local estimates). We will begin by reviewing the theory, reconciling different notations and assumptions, to obtain the equations describing the ambipolar velocity. This includes an elliptical partial differential equation which describes the local deviation from the chemical equilibrium due to the magnetic force. By solving numerically the velocity patterns for given magnetic field topologies, we can identify in which NS region ambipolar diffusion is more important, at which temperature, and what the effect of a superconducting or superfluid phase transition is.

The paper is organized as follows. In Section 2 we review the formalism and the relevant equations. The magnetic field configuration used in the calculations is described in Section 3. Our numerical results for the ambipolar diffusion velocity patterns obtained in different models are presented in Section 4 and we discuss overall timescales in Section 5. In Section 6 we summarize the main conclusions and final remarks.

2 THEORETICAL OVERVIEW

Ambipolar diffusion is a mechanism only present in multicomponent systems. In their seminal work Goldreich & Reisenegger (1992) start from the equations of motion of charged particles in the presence of a magnetic field and a fixed background of neutrons to derive the relevant equations, under a number of simplifying assumptions. A more general description of multifluid magnetohydrodynamics, including the discussion of superfluid and superconducting components is the work of Glampedakis et al. (2011a). The latter reference describes a rigorous covariant formalism to treat general multifluid problems. In our case, we consider a magnetised fluid made of three particle species, protons, electrons and neutrons, respectively. We assume they interact through scattering processes mediated by electromagnetic (charged particles) and nuclear forces (between protons and neutrons), and are subject to β -reactions (weak interactions), and to the gravitational potential.

We are interested in the quasi-stationary evolution driven by slow motions, on timescales much longer than all the relaxation times between collisions of particles of different species. Therefore, we can safely neglect inertial terms in the equations of momentum, as well as terms of order v_i^2 .

We begin by considering the case of a non-rotating neutron star composed of normal (non-superconducting and non-superfluid) matter. To identify the fluid constituents in this work we use Roman letters (x, y). Specifically, we denote neutrons, protons, and electrons with the letters n, p and e , respectively. The three force balance equations, one for each particle species are:

$$\begin{aligned} -\nabla\mu_p - m_p^*\nabla\Phi + e\left(\mathbf{E} + \frac{\mathbf{v}_p}{c} \times \mathbf{B}\right) &= \frac{m_p^*\mathbf{w}_{pn}}{\tau_{pn}} + \frac{m_p^*\mathbf{w}_{pe}}{\tau_{pe}} \\ -\nabla\mu_e - m_e^*\nabla\Phi - e\left(\mathbf{E} + \frac{\mathbf{v}_e}{c} \times \mathbf{B}\right) &= \frac{m_e^*\mathbf{w}_{en}}{\tau_{en}} + \frac{m_e^*\mathbf{w}_{ep}}{\tau_{ep}} \\ -\nabla\mu_n - m_n^*\nabla\Phi &= \frac{m_n^*\mathbf{w}_{np}}{\tau_{np}} + \frac{m_n^*\mathbf{w}_{ne}}{\tau_{ne}} \end{aligned} \quad (1)$$

where \mathbf{E} is the electric field, \mathbf{B} is the magnetic field $\mathbf{w}_{xy} = \mathbf{v}_x - \mathbf{v}_y$ are the relative velocities between the different “fluids”, Φ is the gravitational potential, μ_x the chemical potentials, m_x^* the effective masses, and τ_{xy} is the relaxation time for collisions of x -particles with y -particles. In general, electrons are degenerate relativistic particles in the core of neutron stars, and their effective mass can be considerably larger than their rest mass, $m_e^* = m_e(1 + x_e^2)^{1/2}$, with x_e being the ratio between the Fermi momentum and the electron rest mass $x_e \equiv p_F/m_e c$. On the contrary, the effective masses of neutrons and protons (non-relativistic) contain an interaction contribution that results in effective masses typically smaller than the rest masses $m_n^*/m_n \approx m_p^*/m_p \approx 0.6 - 0.8$. In this work we consider constant effective masses for protons and neutrons with $m_p^* = 0.6 m_p$ and $m_n^* = 0.75 m_n$.

Conservation of momentum implies the conditions $n_x m_x^*/\tau_{xy} = n_y m_y^*/\tau_{xy}$, with n_x denoting the number density of x -type particles. We use the simple description of friction in terms of relaxation times, following Goldreich & Reisenegger (1992), but equivalent expressions can be derived from the more formal equations of Glampedakis et al.

(2011a), which use *entrainment* coefficients to model the coupling between different species.

Combining all three equations to remove the collision terms, one arrives at

$$n_c \nabla(\Delta\mu) + n_b \nabla\mu_n + \rho \nabla\Phi = \frac{\mathbf{j} \times \mathbf{B}}{c}, \quad (2)$$

where we have used the local charge neutrality $n_c \equiv n_e \approx n_p$, while $n_b = n_p + n_n$ is the baryon number density, $\rho = m_p^* n_p + m_n^* n_n + m_e^* n_e$ represents the total mass density, $\mathbf{j} = en_c \mathbf{w}_{pe}$ is the electric current density, and $\Delta\mu \equiv \mu_p + \mu_e - \mu_n$ is the deviation from β -equilibrium. The right hand side is the magnetic force acting on the fluid, which for a non-superconducting star is given by the Lorentz force:

$$\mathbf{f}_{mag} \equiv \frac{\mathbf{j} \times \mathbf{B}}{c}. \quad (3)$$

In a strict magnetostatic equilibrium \mathbf{f}_{mag} must exactly balance the left hand side of equation (2).

The formal derivation of the evolution equations proceeds as follows. First, by combining Eqs. (1), one can work out a general expression of the electric field in terms of the electric current, plus additional terms (generalized Ohm's law), one of which involves a relative velocity between two species. This electric field enters the induction equation describing the evolution of the magnetic field:

$$\frac{\partial \mathbf{B}}{\partial t} = -c \nabla \times \mathbf{E}. \quad (4)$$

In order not to carry on unnecessary coefficients, at this point we note that, for typical neutron star conditions, proton-neutron scattering is mediated by the strong force, while the electrons interact only electromagnetically with the weak neutron magnetic moment. Therefore, we can safely assume that

$$\frac{m_e^*}{\tau_{en}} \ll \frac{m_p^*}{\tau_{pn}}. \quad (5)$$

For simplicity, we also neglect the electron mass (electron contributions to gravitational terms and total momentum).

Then, from the electron momentum equation and the definition of the current, we obtain the following expression for the electric field:

$$\mathbf{E} = \frac{\mathbf{j}}{\sigma_0} - \frac{1}{c} \mathbf{v}_p \times \mathbf{B} + \frac{1}{en_c c} \mathbf{j} \times \mathbf{B} - \frac{1}{e} \nabla \mu_e, \quad (6)$$

where $\sigma_0 = e^2 n_c \tau_{ep} / m_e^*$ is the electrical conductivity in the absence of a magnetic field, which, in the region of validity of equation (5), is dominated by electron-proton collisions. We note that the last term in equation (6) is irrelevant for the induction equation, since its curl vanishes. The first term on the right-hand side is the Ohmic dissipation and the third term is the Hall term, both of which are very important in the NS crust, but are negligible in the core.

If we define the average baryon velocity by

$$\mathbf{v}_b = \frac{n_n \mathbf{v}_n + n_p \mathbf{v}_p}{n_b}, \quad (7)$$

we can rewrite the second term on the right hand side as

$$\mathbf{v}_p \times \mathbf{B} = \mathbf{v}_b \times \mathbf{B} + x_n \mathbf{w}_{pn} \times \mathbf{B}, \quad (8)$$

where $x_n = n_n / n_b$ is the neutron fraction. In this form, we can identify the advective term due to the hydrodynamic velocity of baryons, which should be negligible if we are very

close to dynamical equilibrium, and the second term, the *ambipolar diffusion*, due to relative velocity between protons and neutrons. Note that ambipolar diffusion becomes dominant over the Hall term when protons and electrons are strongly coupled, with their velocity difference being much smaller than their individual velocities. Therefore, our problem can be reduced to a two-fluid model consisting of a neutral component and a charged fluid (protons plus electrons, moving with nearly the same speed) locked to the magnetic field. If the charged and neutral components are also locked to each other, there is only a single hydrodynamic velocity and we recover the one-fluid MHD limit.

2.1 Ambipolar drift velocity

We now discuss how to estimate the ambipolar diffusion velocity, $\mathbf{v}_{amb} \equiv x_n \mathbf{w}_{pn}$. Combining the three equations (1) to remove the electric field and using equation (5), we have:

$$\frac{\mathbf{f}_{mag}}{n_c} - \nabla(\Delta\mu) = \frac{1}{x_n^2} \frac{m_p^* \mathbf{v}_{amb}}{\tau_{pn}}. \quad (9)$$

If β -reactions are fast, bringing the fluid to chemical equilibrium ($\Delta\mu = 0$), Equation (9) shows that there is a quasi-stationary, slow motion of the charged component with respect to the neutron fluid, proportional to the Lorentz force, simply

$$\mathbf{v}_{amb} = x_n^2 \frac{\tau_{pn}}{m_p^*} \frac{\mathbf{f}_{mag}}{n_c}. \quad (10)$$

Equation (9) also shows that, if β -equilibrium is not reached faster than the evolution timescale, the magnetic force per charged particle can be partially balanced by the pressure gradients induced by small deviations from β -equilibrium. However, we note that only the irrotational part of \mathbf{f}_{mag}/n_c can be cancelled by a gradient term, the solenoidal part remains unbalanced resulting in a finite ambipolar velocity (see Appendix B for more details on the irrotational-solenoidal decomposition of a vector field).

In order to determine the ambipolar velocity in the general case, we need to calculate the chemical deviation $\Delta\mu$ throughout the star. For this purpose, we must also consider the individual continuity equations and, since we search for quasi-stationary solutions, we can neglect the time variation of the number densities to write:

$$\begin{aligned} \nabla \cdot (n_p \mathbf{v}_p) &= -\Delta\Gamma, \\ \nabla \cdot (n_e \mathbf{v}_e) &= -\Delta\Gamma, \\ \nabla \cdot (n_n \mathbf{v}_n) &= \Delta\Gamma. \end{aligned} \quad (11)$$

where

$$\Delta\Gamma = \Gamma(p + e \rightarrow n + \nu_e) - \Gamma(n \rightarrow p + e + \bar{\nu}_e), \quad (12)$$

with Γ denoting the reaction rate. When $\Delta\mu \ll k_B T$, the reaction rates can be linearized and written in terms of the deviation from chemical equilibrium as follows:

$$\Delta\Gamma = \lambda \Delta\mu, \quad (13)$$

where $\lambda \equiv (d\Gamma/d\Delta\mu)|_{eq}$ is a coefficient which depends on the density and temperature. If $\Delta\mu \gtrsim k_B T$, nonlinear terms in the β -reaction rates should be considered.

Taking the divergence of Eq. (9) and making use of the

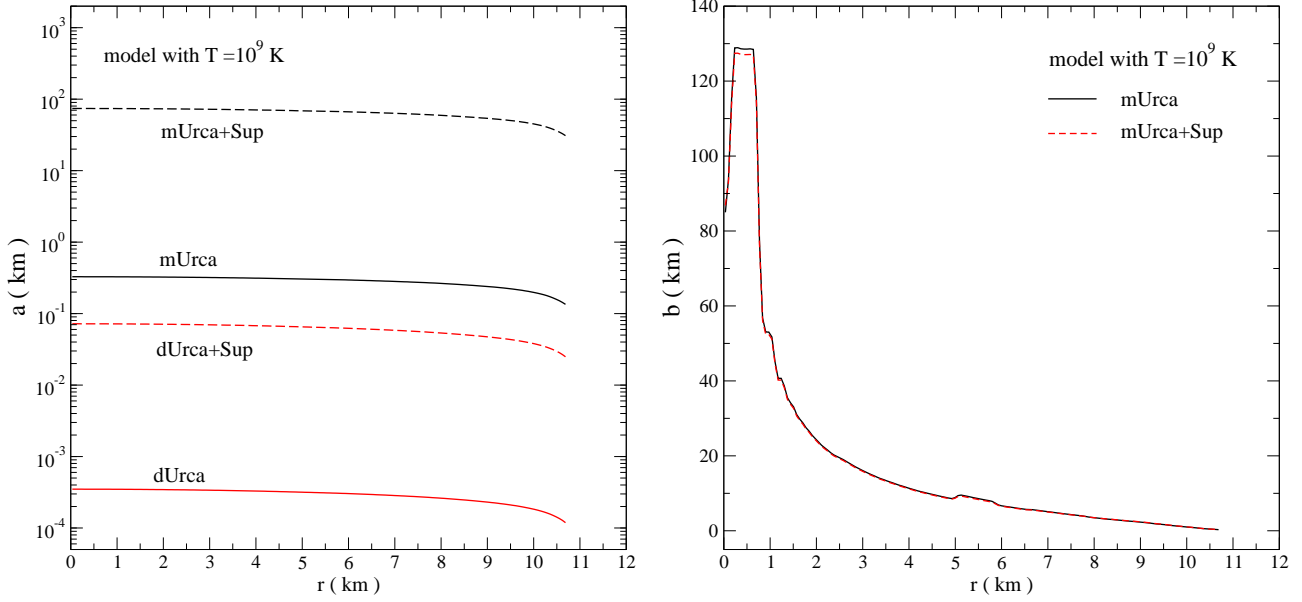


Figure 1. Radial profiles of the coefficients a and b (see Eq. 15) for a star with $T = 10^9$ K. The left-hand panel displays the coefficient a , on logarithmic scale, for stellar models with normal (solid lines) and superfluid/superconducting matter (dashed lines) and for mUrca (black lines) and dUrca reactions (red lines). The right-hand panel shows the coefficient b for a star with mUrca reactions and with normal (solid-black line) and superfluid/superconducting (dashed-red line) matter. In this figure the superconducting model has $T_{cp} = 5 \times 10^9$ K and $T_{cn} = 10^9$ K.

continuity Eqs. (11), we can obtain the following elliptic equation for the chemical equilibrium deviation $\Delta\mu$:

$$\nabla^2(\Delta\mu) - \frac{1}{b} \frac{\partial \Delta\mu}{\partial r} - \frac{1}{a^2} \Delta\mu = \nabla \cdot \left(\frac{\mathbf{f}_{mag}}{n_c} \right) - \frac{1}{b} \frac{f_{mag}^r}{n_c}, \quad (14)$$

where we have defined

$$\frac{1}{a^2} = \frac{\lambda m_p^*}{x_n^2 n_c \tau_{pn}}, \quad \frac{1}{b} = \frac{d}{dr} \ln \left(\frac{m_p^*}{x_n n_c \tau_{pn}} \right). \quad (15)$$

Both a and b have dimensions of length. In Appendix A we give more details about the derivation of equation (14) and the approximations involved. To summarize, for a given magnetic field configuration we can calculate \mathbf{v}_{amb} from equation (9), where $\Delta\mu$ is obtained by solving numerically equation (14) in the domain $0 \leq r \leq R_{cc}$ and $0 \leq \theta \leq \pi$, where R_{cc} denotes the position of the crust/core interface. As boundary conditions, we impose that the ambipolar velocity satisfies the regularity conditions at the origin and the magnetic axis. At the crust-core interface, ($r = R_{cc}$), we impose that the radial component of the velocity vanishes, which is equivalent to:

$$\frac{\partial \Delta\mu}{\partial r} - \frac{f_{mag}^r}{n_c} = 0. \quad (16)$$

This boundary condition is easily satisfied when $\Delta\mu$ is not negligible. On the other hand, at high temperatures, $T \sim 10^9$ K, β -reactions quickly smooth out deviations from equilibrium and a discontinuity (or a sharp gradient) in $\Delta\mu$ is developed at the crust-core interface, if the magnetic force does not vanish there. Some numerical tests of the solutions against analytical models are presented in Appendix B.

As for the microphysics input, for normal matter, we adopt the proton-neutron collision time, τ_{pn} , from Yakovlev

& Shalybkov (1990):

$$\frac{1}{\tau_{pn}} = 4.7 \times 10^{16} T_8^2 \left(\frac{\rho}{\rho_{nuc}} \right)^{-1/3} \text{ s}^{-1}, \quad (17)$$

where T_8 is the temperature in units of 10^8 K, and $\rho_{nuc} = 2.8 \times 10^{14} \text{ g cm}^{-3}$ is the nuclear saturation density.

In the neutron star interior, weak interactions are driven by two types of Urca reactions. The most common channel is the modified Urca (mUrca), which allows the conservation of energy and momentum with the help of a spectator nucleon. In very compact stars, if the proton fraction $x_p \gtrsim 0.11$, β -reactions could be much faster through the activation of direct Urca (dUrca) processes, without the support of spectator nucleons (Lattimer et al. 1991). We will use the mUrca reaction rates given by Sawyer (1989):

$$\lambda = 5 \times 10^{27} T_8^6 \left(\frac{\rho}{\rho_{nuc}} \right)^{2/3} \text{ ergs}^{-1} \text{ cm}^{-3} \text{ s}^{-1}, \quad (18)$$

and the dUrca rates obtained by Haensel & Schaeffer (1992)

$$\lambda = 3.5 \times 10^{36} \frac{m_n^* m_p^*}{m_n m_p} T_8^4 \left(\frac{\rho_c}{\rho_{nuc}} \right)^{1/3} \text{ ergs}^{-1} \text{ cm}^{-3} \text{ s}^{-1}. \quad (19)$$

2.2 Superfluidity and Superconductivity

After a neutron star cools down below the critical temperatures T_{cn} and T_{cp} , the neutrons and protons in the core are, respectively, in a superfluid and superconducting state. In a type II superconductor, the magnetic field permeates the core with an array of quantised fluxtubes, while neutron vortices sustain the star's rotation. Collision rates and β -reaction rates decrease considerably with respect to the normal matter case, and new dissipative processes mediated by vortices may appear. Since we are interested in strong

magnetic fields (and therefore slowly rotating stars), we neglect the effects of neutron vortices on the long term evolution. In other words, we are in the hot superfluid regime studied by Glampedakis et al. (2011b) ($T \gtrsim 3 \times 10^8 \text{K}$) in which particle scattering is dominant over the dissipation due to mutual friction between fluxoids and vortices.

Under this assumption, we introduce the superfluidity and superconductivity effects in our analysis by considering the corrections to both the relaxation timescale τ_{pn} and the weak reaction rate λ , which are usually expressed in terms of suppression factors, respectively \mathcal{R}_{pn} and \mathcal{R}_{sup} , which become exponentially small in the strong superfluid regime $T \ll T_{\text{cx}}$. In general, the suppression factors depend on the gap model and are described by complex integrals, whose results have been fitted to more practical analytical formulae (Levenfish & Yakovlev 1994; Yakovlev & Levenfish 1995; Haensel et al. 2000, 2001). From these references, we take the appropriate suppression factors to modify the rates as follows:

$$\frac{1}{\tau_{\text{pn}}} \longrightarrow \frac{\mathcal{R}_{\text{pn}}}{\tau_{\text{pn}}}, \quad (20)$$

$$\lambda \longrightarrow \lambda \mathcal{R}_{\text{sup}}, \quad (21)$$

and consequently the coefficients of Eqs. (9) and (14).

We also consider the superconductivity effects on the force by replacing the Lorentz force with the magnetic force for a type II superconductor (Akgün & Wasserman 2008; Glampedakis et al. 2011a,b):

$$\mathbf{f}_{\text{mag}} = \frac{1}{4\pi} \left(\nabla \times H_{c1} \hat{\mathbf{B}} \right) \times \mathbf{B} - \frac{n_c}{4\pi} \nabla \left(B \frac{\partial H_{c1}}{\partial n_p} \right), \quad (22)$$

where $\hat{\mathbf{B}} = \mathbf{B}/B$ is the unit vector in the direction of the magnetic field, and H_{c1} is the lower critical field (Tinkham 2004). In typical conditions of type II superconductivity in NSs

$$H_{c1} \approx 10^{15} \left(\frac{n_p}{0.01 \text{ fm}^{-3}} \right) \text{ G}. \quad (23)$$

The radial profiles of the coefficients a and b defined in equation (15) are shown in Fig. 1 for different states of matter (normal and superfluid/superconducting) and weak reaction processes (mUrca and dUrca). The stellar model is built with the same equation of state as in Viganò et al. (2013), and its parameters are $M = 1.4M_{\odot}$, $R = 11.6 \text{ km}$, while the crust/core interface is at $R_{\text{cc}} = 10.79 \text{ km}$. As an illustrative example we show the results for a star with $T = 10^9 \text{ K}$ and with a constant gap model described by $T_{\text{cp}} = 5 \times 10^9 \text{ K}$ and $T_{\text{cn}} = 10^9 \text{ K}$. The left-hand panel of Fig. 1 shows the strong dependence of a on the β -reaction process. Its value for mUrca reactions is about three orders of magnitude larger than the dUrca case. In the same figure we can notice the effects of the superconducting transition and thus of the suppression factors \mathcal{R}_{pn} and \mathcal{R}_{sup} , which increase a for more than two orders of magnitude. When $T \ll T_{\text{cp}}$, the effects of the suppression factors are even more relevant due to their exponential dependence on the temperature. The quantity b does not depend on λ and thus it is not affected by the particular β -reaction process. Hence, we show in the right-hand panel of Fig. 1 the profile of b for the mUrca reactions and for normal and superconducting matter. Since \mathcal{R}_{pn} is almost constant for the gap model used in this work, the \mathcal{R}_{pn} has a tiny effect on b . For stars

in a non superfluid/superconducting state, the variation of a and b with the temperature can be easily determined by equations (15) and (17)-(19).

3 MAGNETIC FIELD CONFIGURATION

The actual geometry of the magnetic field inside a neutron star is unknown. For practical purposes, we will consider an analytical, axisymmetric model which satisfies the relevant boundary and regularity conditions.

Any axisymmetric magnetic field can be decomposed into poloidal and toroidal components as follows (Chandrasekhar 1961)

$$\mathbf{B} = \frac{1}{r \sin \theta} \left(\nabla \mathcal{P} \times \hat{\phi} + \mathcal{T} \hat{\phi} \right). \quad (24)$$

Here $\mathcal{P}(r, \theta)$ and $\mathcal{T}(r, \theta)$ are, respectively, the poloidal and toroidal stream functions, and $\hat{\phi}$ is the unit vector in the azimuthal direction. In a barotropic fluid in MHD equilibrium, these functions must be solutions of the Grad-Shafranov equation, and the Lorentz force can be expressed as the mass density times the gradient of a (magnetic) potential, $\mathbf{f}_{\text{mag}} = \rho \nabla \mathcal{M}(\mathcal{P})$, where \mathcal{M} is some arbitrary function of \mathcal{P} . In this case $\mathbf{f}_{\text{mag}}/\rho$ is a purely irrotational quantity. On the other hand, in a non-barotropic star the quantity $\mathbf{f}_{\text{mag}}/\rho$ is not necessarily a gradient of a potential, and the poloidal and toroidal functions can be chosen with more flexibility. Thus, we adopt the simple magnetic field model constructed for non-barotropic fluids in Akgün et al. (2013).

We consider a mixed poloidal-toroidal configuration which smoothly joins to a vacuum dipole solution at the star's surface. We choose a dipolar poloidal function of the form

$$\mathcal{P}(r, \theta) = \mathcal{P}_0 f(x) \sin^2 \theta, \quad (25)$$

where \mathcal{P}_0 is a constant that sets the poloidal field amplitude, and x is a dimensionless radial coordinate defined through $x = r/R_{\star}$, with R_{\star} being the radius where the field continuously joins the vacuum solution. In this work, R_{\star} is taken as the stellar radius. Outside the star, where there are no currents, the dipole vacuum solution must satisfy

$$f_{\text{out}}(x) \propto x^{-1}. \quad (26)$$

On the other hand, the interior dipolar field is assumed to be a polynomial of order n

$$f_{\text{in}}(x) = \sum_{i=1}^n f_i x^i, \quad (27)$$

where f_i are coefficients to be determined from regularity conditions at the center and boundary conditions at the surface. These conditions imply that the function f_{in} must have at least three terms; in particular, we take the first three even terms in the power series (see Akgün et al. 2013, for a detailed discussion of the regularity and boundary conditions). Thus, the radial function can be written as

$$f(x) = \begin{cases} f_2 x^2 + f_4 x^4 + f_6 x^6 & \text{for } x < 1, \\ x^{-1} & \text{for } x \geq 1, \end{cases} \quad (28)$$

where the vacuum solution is normalized so that $f(1) = 1$. The three unknown coefficients are determined from the

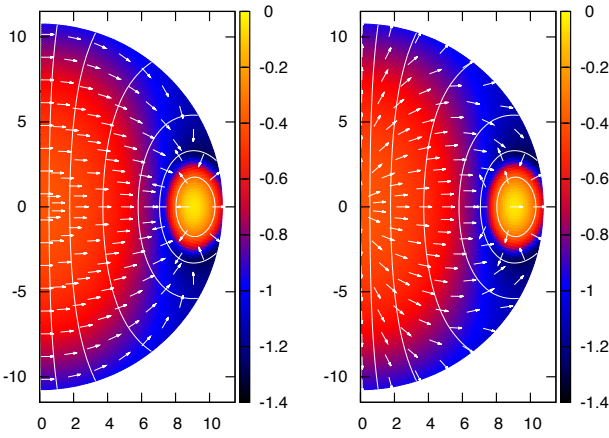


Figure 2. Configuration of the magnetic field and the magnetic force. The colors denote the strength of the magnetic field magnitude in logarithmic scale, $\log [B / (10^{15} \text{G})]$, the white-solid curves show the projection of the poloidal magnetic field lines, while the arrows represent the direction of the magnetic force. In the two panels, the magnetic field has the same mixed poloidal-toroidal geometry with $\mathcal{P}_c = \mathcal{P}_0$. The magnetic force is the usual Lorentz force (left-hand panel) and superconducting force (right-hand panel). In the horizontal and vertical axes (left), the units are given in km.

boundary conditions at $x = 1$ for the continuity of the magnetic field and the vanishing of the current, which can now be expressed as

$$f'(1) = -f(1) \quad \text{and} \quad f''(1) = 2f(1). \quad (29)$$

The coefficients which satisfy these boundary conditions are given by

$$f_2 = \frac{35}{8}, \quad f_4 = -\frac{21}{4} \quad \text{and} \quad f_6 = \frac{15}{8}. \quad (30)$$

We take the toroidal component of the magnetic field to be described by a toroidal function $\mathcal{T}(\mathcal{P})$ which is confined to the closed field lines within the radius $x = 1$. This assumption implies that the azimuthal component of the Lorentz force vanishes. Following the notation of Akgün et al. (2016), we choose

$$\mathcal{T}(\mathcal{P}) = \begin{cases} s(\mathcal{P} - \mathcal{P}_c)^\sigma & \text{for } \mathcal{P} \geq \mathcal{P}_c, \\ 0 & \text{for } \mathcal{P} < \mathcal{P}_c. \end{cases} \quad (31)$$

where s is a constant that sets the amplitude of the toroidal field with respect to the poloidal field, σ is a constant that defines the relation between the functions \mathcal{T} and \mathcal{P} , and \mathcal{P}_c defines the field line which encloses the toroidal field. In this work, we choose \mathcal{P}_c to be equal to the maximum value of the function \mathcal{P} at the stellar surface, i.e. $\mathcal{P}_c = \mathcal{P}_0$. In order to avoid surface currents we must have $\sigma \geq 1$. Moreover, to ensure the continuity of the gradient of the Lorentz force across the toroidal boundary, we set $\sigma = 2$.

As described in Sec. 2.2, when the star is superconducting we replace the Lorentz force with the superconducting magnetic force. Nevertheless, we still use the same magnetic field configuration described in this section. Although this approach is not strictly correct, for the purposes of this work we prefer to maintain here the same magnetic field configuration in order to isolate the effects of a different superconducting force and the reduced collision rates on the velocity

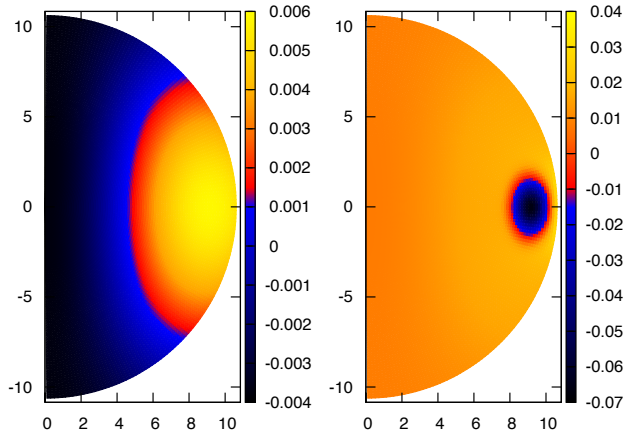


Figure 3. Two-dimensional contour plots of the quantity $\Delta\mu/k_B T$ for a normal matter star, with mUrca neutrino processes, and $T = 2 \times 10^8 \text{K}$. The left and right-hand panels show, respectively, the solution for a purely poloidal field (model A) and for a mixed poloidal-toroidal field (model B). In the horizontal and vertical axes (left), the units are given in km.

pattern. A further effect related to the change of magnetic topology in models with superconducting cores (Roberts 1981; Henriksson & Wasserman 2013; Lander 2013, 2014) will be addressed in the future. In this work, our purpose is to give quantitative estimates for the different possible scenarios.

For a mixed poloidal-toroidal configuration, with 10^{14}G at the pole and a toroidal field with maximum strength 10^{15}G , we show in Fig. 2 the magnetic field amplitude and its field lines as well as the direction of the Lorentz (left-hand panel) and superconducting (right-hand panel) forces. Obviously, the choice of the initial configuration determines the value of the Lorentz force and therefore v_{amb} .

4 RESULTS

In this section, we present our results for the axisymmetric magnetic field configuration described in Sec. 3. The neutron star model is built with the same equation of state and parameters as in Viganò et al. (2013) ($M = 1.4M_\odot$, $R = 11.6 \text{ km}$ and $R_{cc} = 10.79 \text{ km}$). We consider two magnetic field models: i) a purely poloidal magnetic field with $B_p = 10^{14} \text{G}$ at the pole (hereafter model A); ii) a mixed poloidal-toroidal magnetic field with $B_p = 10^{14} \text{G}$ and a toroidal field with maximum strength $B_t = 10^{15} \text{G}$ (hereafter model B). We explore the temperature interval $10^7 \text{K} \leq T \leq 2 \times 10^9 \text{K}$, which covers the expected core temperatures in a NS from $1 - 10^6$ years. Note that the core becomes nearly isothermal (except for gravitational redshift corrections) only minutes after birth, and that important thermal gradients are only present in the envelope and to a lesser extent in the crust, in presence of strong magnetic fields. We also remind that this internal temperature is not the surface temperature, which is typically two orders of magnitude smaller. We consider both normal and superfluid/superconducting matter and discuss the differences between the standard cooling scenario (mUrca reactions) and the fast cooling scenario (dUrca processes).

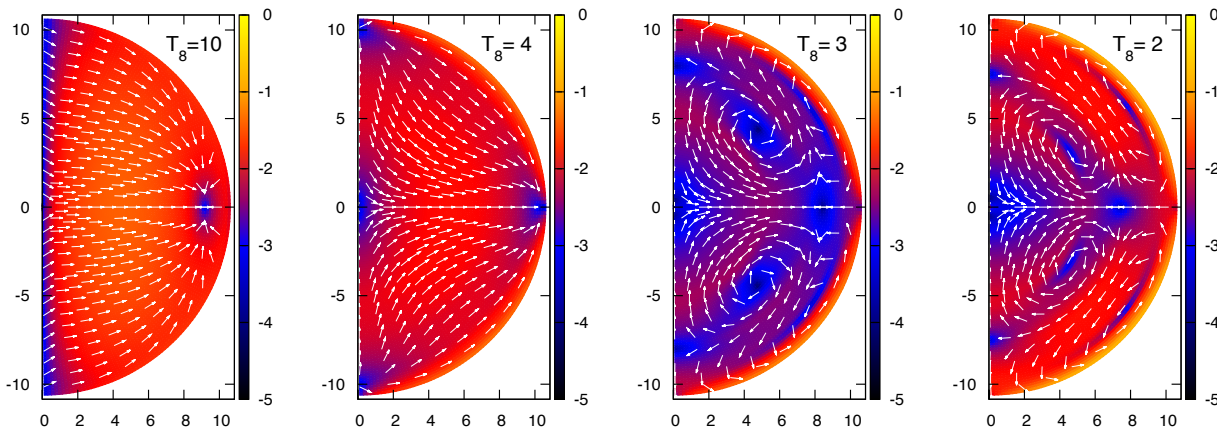


Figure 4. Ambipolar diffusion velocity (v_{amb}) in a non-superfluid/superconducting core with mUrca processes at different temperatures. From the left to right: $T_8 = 10, 4, 3$ and 2 . The magnetic field is given by model A (purely poloidal field). The arrows show the direction of the velocity field and the color scale represents $\log |v_{amb}|$, where velocities are given in km/Myr. In the horizontal and vertical axes (left), the units are given in km.

To derive equation (14) we have approximated the β -reaction rate with equation (13). However, this relation is strictly valid only at first order, i.e. when $\Delta\mu \ll k_B T$. An example of two typical solutions of equation (14) is given in Fig. 3, which shows $\Delta\mu/k_B T$ for a non-superfluid star with mUrca processes at the temperature $T = 2 \times 10^8$ K, and for both model A (left panel) and B (right panel). For these particular cases, the ‘linear’ approximation is still valid for 2×10^8 K. The temperature range, in which this approximation holds, depends on the weak interaction process (dUrca or mUrca), on the state of core nucleons (normal or superfluid/superconducting) and on the magnetic field strength. In the following sections, we will provide the results only for models in which $\Delta\mu \ll k_B T$ is satisfied.

4.1 Normal matter

We begin our analysis with a non-superfluid/non-superconducting neutron star core, where the weak interactions occur only through the mUrca process. For the purely poloidal case (model A), we show in Fig. 4 the 2D pattern of the ambipolar velocity for a selection of four different temperatures, respectively, $T_8 = 10, 4, 3$ and 2 (where T_8 is the temperature in units of 10^8 K). At high temperature, the chemical reactions are very fast and $\Delta\mu$ is negligible. The ambipolar velocity is proportional to the Lorentz force, and it exhibits a dominant irrotational pattern with the flow advecting the magnetic field away from the axis, and locally converging toward the nodal line of the poloidal magnetic field. As the temperature decreases, when the mUrca processes are not fast enough to establish β -equilibrium, the chemical gradients partially cancel the Lorentz force, more precisely, the irrotational component of the \mathbf{f}_{mag}/n_c vector (see the Helmholtz-Hodge decomposition in Appendix B for more details), and the velocity pattern is modified. The transition from an irrotational-dominated flow to a solenoidal-dominated flow (see the third and fourth panel of Fig. 4) is clearly observed, with two vorticity zones in each hemisphere, a narrower one close to the crust/core interface and a second wider zone in the interior. As expected from the

temperature dependence of τ_{pn} , the speed of the ambipolar diffusion is larger at lower temperatures. In particular, we find that the ambipolar flow is faster near the crust/core interface where one of the vorticity zones is present.

The results for the mixed-magnetic field (model B) are shown in Fig. 5. The qualitative properties of the velocity pattern are similar to the purely poloidal case: transition from a (high T) non-solenoidal flow to a (low T) solenoidal flow. However, there are also some interesting differences. First, the largest speed is now reached in the toroidal magnetic field region, which simply reflects our choice $B_t > B_p$. More interestingly, combined with the advection of poloidal field lines away from the axis, we see the expansion of the region containing the toroidal field. In some regions, these two flows are opposite, which in a real evolution model should result in a compression of magnetic field lines. This pattern structure is particularly evident at high temperature (see the first panel from the left of Fig. 5). For lower T , the ‘toroidal’ flow extends further toward the stellar interior (second and third panel of Fig. 5), until the chemical gradients become strong enough to balance the irrotational part of \mathbf{f}_{mag}/n_c . At $T_8 = 2$ a clear solenoidal flow emerges again, mainly in the region with the toroidal magnetic field.

If the central density of the star is sufficiently high to allow the dUrca channel (or other fast neutrino processes), β -equilibrium is quickly re-established. In Fig. 6 we show the results for normal matter with dUrca processes and mixed-magnetic field (model B). This should only happen in very massive stars, and in a fraction of the core volume, but we prefer to show results with the same neutron star model and considering fast neutrino reactions in the whole core to better illustrate the differences. At $T_8 = 1$, the irrotational pattern of the flow is still dominant, while at lower temperatures $\Delta\mu$ begins to affect the solution. The transition to a mainly solenoidal velocity pattern occurs for temperatures below 4×10^7 K (see the right-hand panel of Fig. 6). Note that the flow speed is now much higher, reaching values of about 10^2 - 10^3 km/Myr in some regions. This means that ambipolar diffusion can have an important effect in more massive neutron stars, on timescales of kyr. However, in the

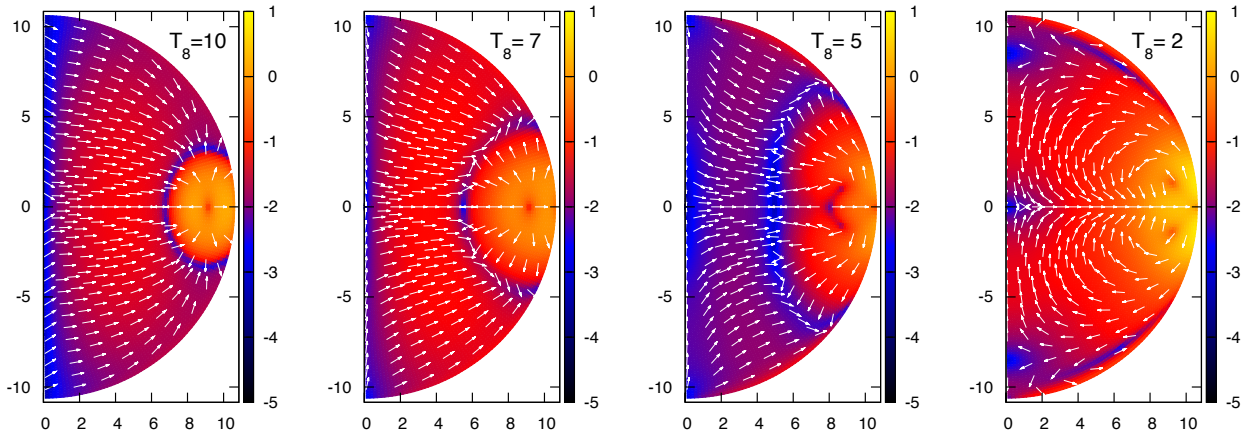


Figure 5. Same as Fig. 4, for $T_8 = 10, 7, 5$ and 2 , but for a magnetic field described by model B (mixed poloidal-toroidal magnetic field).

fast cooling scenario with dUrca processes, the star also cools much rapidly and it remains to be proven by detailed simulations if significant magnetic diffusion can occur before the star becomes too cold.

4.2 Superfluid/superconducting matter

A realistic neutron star is expected to become superfluid and superconducting, resulting in very different timescales compared to the normal matter case. This is mainly due to the suppression of the proton and neutron collision and β -reaction rates, especially in the strong superfluid regime. As described in Sec. 2.2, we include the superfluid/superconducting correction on the reaction rates and replace the Lorentz force with the superconducting magnetic force.

To avoid the coexistence of normal and superconducting regions inside the star and thus in our numerical domain, we consider constant gap models, i.e. T_{cx} independent of density. In fact, it is not clear how to handle, macroscopically, regions where the magnetic force changes from normal to superconducting states. This transition is likely not sharp and occurs in an intermediate layer where superconducting fluxtubes should gradually join the magnetic field in a normal state. Essentially, in our model, we use the Lorentz force when $T > T_{cp}$ and the superconducting force when $T \leq T_{cp}$. For the superfluid/superconducting case we discuss only the mixed-magnetic field configuration given by model B.

In Fig. 7 we show the results for a neutron star with mUrca reactions and with critical temperatures given by $T_{cp} = 5 \times 10^9$ K and $T_{cn} = 10^9$ K, respectively. This choice is consistent with the theoretical calculations, which predict a higher transition temperature for protons. During the cooling of a neutron star, we therefore expect that the superconducting transition sets in earlier than the superfluid transition of neutrons. One of the main effects of the superconducting/superfluid transition is that the suppression of the irrotational part of the Lorentz force by the chemical gradients occurs at higher temperature with respect to the normal case, because of the longer reaction rate of the β -equilibrium processes. Comparing Fig. 7 to Fig. 5, we clearly see that when the temperature is $T_8 = 9$ the ambipolar ve-

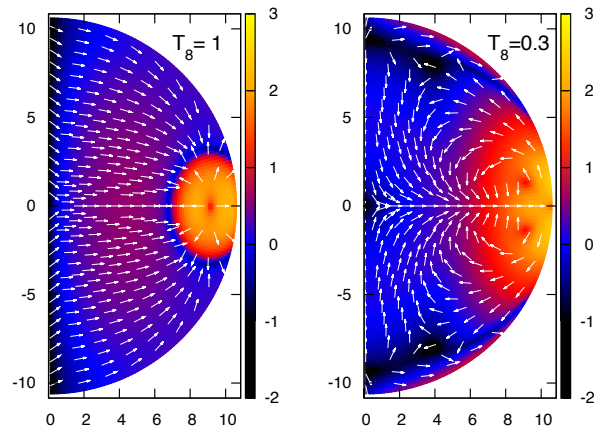


Figure 6. Same as Fig. 4, for $T_8 = 1$ and 0.3 , but with the magnetic field of model B and for a neutron star core with dUrca reactions.

locity is already dominated by the solenoidal mode, with two large vorticity zones. More interestingly, the ambipolar flow now reaches a very high speed of $\sim 10^3$ km/Myr. Differently from the non-superfluid case, the maximum of v_{amb} is not only restricted into the closed field line region but it is large also outside, in a wide spherical shell. This effect is in part due to the different form of the magnetic force, that scales with $H_{c1}B$ instead of B^2 .

Certainly, the temperature at which the solution becomes mostly solenoidal depends on the particular choice of T_{cp} and T_{cn} . We have explored different critical temperatures T_{cx} , the ambipolar diffusion pattern is similar to what just described, but the transition to a solenoidal velocity occurs at different T . We will return to this point in the next section.

If dUrca reactions are activated, the chemical gradients begin to balance the irrotational part of \mathbf{f}_{mag}/n_c when $T_8 \lesssim 8$. We show in Fig. 8, the velocity pattern for two cases, respectively, at $T_8 = 7.2$ (left-hand panel) and $T_8 = 5.4$ (right-hand panel). In the former case, $\Delta\mu$ begins to affect the velocity, while in the latter the characteristic vorticity zones become visible. The most interesting result is that

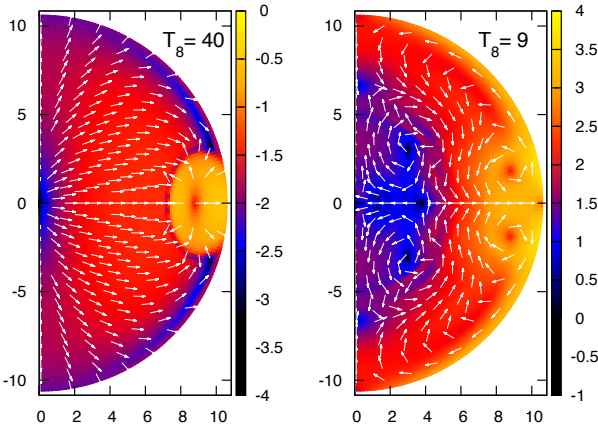


Figure 7. Same as Fig. 4, for a superfluid/superconducting star with the magnetic field described by model B and mUrca processes. We show results for $T_8 = 40$ and 9, from left to right.

this particular case (superfluid/superconducting star with fast neutrino cooling processes) results in the largest velocities, up to $10^6 - 10^8$ km/Myr in the temperature interval $5 < T_8 < 7$. The impact on the magnetic field evolution is therefore potentially strong. The rapid cooling induced by dUrca reactions can however moderate the effects of this high speed. A conclusive answer can be only given when the ambipolar drift is consistently incorporated in simulations of the magneto-thermal evolution. This issue will be addressed in a future work.

5 TIMESCALES

We now discuss the timescales associated with ambipolar diffusion and compare our results with the analytical estimates given in the literature. From the numerical solutions we determine two different timescales. The first is defined by the following equation:

$$t_{amb} = \frac{L}{\langle v_{amb} \rangle}, \quad (32)$$

where L is a typical distance in which the magnetic field varies, and $\langle v_{amb} \rangle$ is the volume average of the velocity modulus. Equation (32) provides an average timescale on which a magnetic field line is advected to a distance L by a velocity v_{amb} . This may or may not result in field dissipation. To study the magnetic field dissipation rate, we also introduce the following timescale:

$$t_B = -\frac{2E_B}{\dot{E}_B}, \quad (33)$$

where E_B and \dot{E}_B are, respectively, the magnetic energy and the energy dissipation rate due to ambipolar velocity (the dot denotes a time derivative). For normal matter, these quantities read (Goldreich & Reisenegger 1992)

$$E_B = \frac{1}{8\pi} \int dV B^2, \quad (34)$$

$$\dot{E}_B = - \int dV \mathbf{v}_{amb} \cdot \mathbf{f}_{mag}. \quad (35)$$

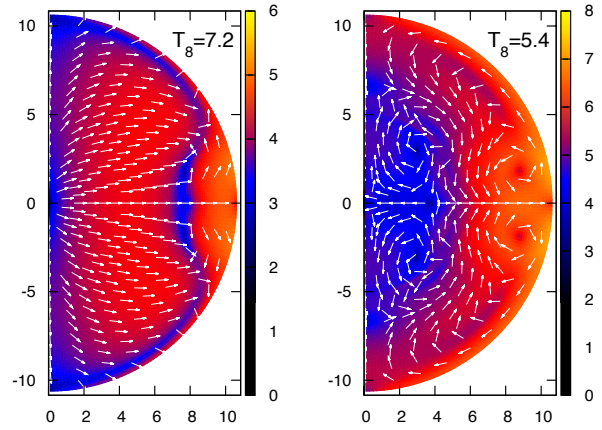


Figure 8. Same as Fig. 7 but for a star with dUrca reactions, and $T_8 = 7.2$ and 5.4.

To determine equation (33), we have assumed that the time dependence of the magnetic field is $B \sim e^{-t/t_B}$. We note that a large v_{amb} that is nearly perpendicular to the Lorentz force gives a fast evolution of the magnetic field, t_{amb} , but without dissipation. For superconducting stars we do not determine the timescale t_B , as the analogous to Eq. (35) contains also surface terms which are not negligible. These terms strongly depend on the matching conditions imposed at the interface separating the superconducting and normal states.

In our numerical approach, we do not separate explicitly between solenoidal and irrotational components, therefore t_{amb} and t_B describe global timescales. By using the Helmholtz-Hodge decomposition of the velocity and magnetic force, Goldreich & Reisenegger (1992) found the following analytical estimates for the solenoidal and irrotational ambipolar diffusion timescales:

$$t^{sol} \sim \frac{4\pi m_p^* n_c L^2}{\tau_{pn} B^2}, \quad t^{irr} \sim t^{sol} \left(1 + \frac{a^2}{L^2} \right), \quad (36)$$

where a is the coefficient defined in equation (15)¹, and we have replaced m_p with an effective proton mass m_p^* . At high temperature, $a \ll L$ and the two timescales are almost the same. At low T , the chemical gradients suppress the irrotational part of the force and $t^{sol} \ll t^{irr}$. To calculate these analytical quantities, we specify a typical L and determine t^{irr} and t^{sol} in the entire numerical grid, and then extract either their minimum or their volume average value.

In Fig. 9, we show the temperature dependence of the ambipolar diffusion timescales for a stellar model with normal matter, mUrca reactions, and a magnetic field described by model B. We use $L = 1$ km to determine the volume average of t_{amb} , t^{sol} and t^{irr} . The two analytical timescales almost coincide, as expected, at high temperature, while they start to diverge when $T_8 \lesssim 10$. The solenoidal timescale reflects the T^2 dependence of τ_{pn}^{-1} , while the irrotational timescale, when $a \gg L$, becomes independent of L and scales as λ^{-1} (T^{-6} and T^{-4} for mUrca and dUrca processes, respectively).

¹ In Goldreich & Reisenegger (1992), the coefficient a is defined as in Eq. (15) but with $x_n = 1$.

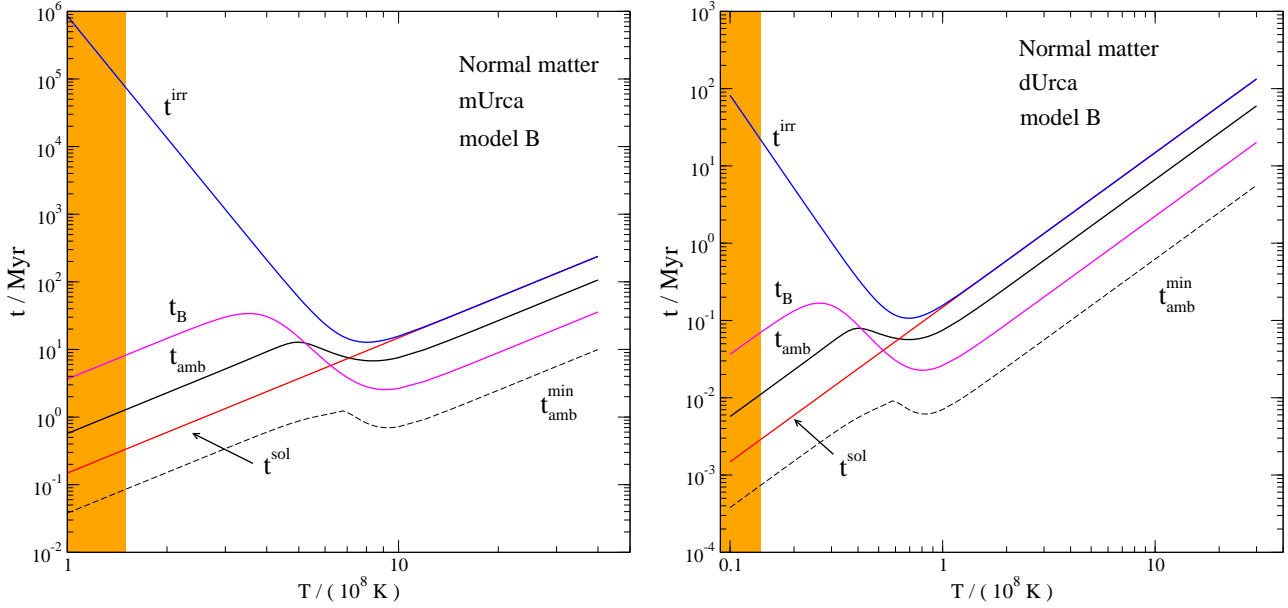


Figure 9. Ambipolar diffusion timescales as a function of temperature for normal matter and model B. The left panel shows results assuming mUrca reactions and the right panel for dUrca processes. The black, red and blue solid lines, respectively, denote the volume average of the t_{amb} , t^{sol} and t^{irr} timescale for $L = 1$ km. The black-dashed line refers to the minimum of t_{amb} , while the magenta-solid line shows t_B . The orange region delimits the temperature range where the condition $\Delta\mu \ll k_B T$ is not satisfied.

Our numerical results agree, within an order of magnitude, with the analytical estimates, but with some interesting differences. The numerical t_{amb} shows the correct temperature scaling (T^2) at high and low temperature, with a bump indicating the transition to solenoidal flow at $5 < T_8 < 10$. Note that the large timescales predicted by the irrotational mode estimates at low temperature will never be realized in a real scenario. That would require to construct a magnetic field configuration such that the Lorentz force per charged particle is a purely irrotational vector. In any other case, there will be a non-vanishing solenoidal part that determines the actual timescale of ambipolar diffusion. We only see the temperature scaling corresponding to the irrotational mode in the transition temperature interval, while $\Delta\mu$ is growing to balance the irrotational part of the \mathbf{f}_{mag}/n_c vector. However, the presence of a solenoidal part limits the increase of t_{amb} and, for $T_8 < 5$, it follows again the T^2 scaling. The transition to a predominant solenoidal solution always shows this characteristic S-shape. The dissipation timescale t_B is also shown in Fig. 9. It follows the same qualitative behaviour as t_{amb} but with a wider variation. At high temperature the velocity and the magnetic force are always parallel, which maximizes \dot{E}_B , resulting in short diffusion timescales. At low T , when the solenoidal flow dominates, the Lorentz force and the velocity field are no longer aligned, which explains why at $T_8 < 3$ we find $t_B > t_{amb}$.

For the same stellar model we also consider the case of dUrca reactions (right panel). The results are similar, except that the transition now appears at $0.4 < T_8 < 0.8$, at a temperature which is roughly one order of magnitude smaller than the mUrca case, due to the enhanced efficiency of the β -reaction rates.

Our results show that for the mUrca case, in the temperature range $1 \leq T_8 \leq 10$, t_{amb} is larger than 1 Myr. This

value decreases by an order of magnitude if we consider the minimum numerical timescale t_{amb}^{min} (shown as a dashed-line in Fig. 9), but this is only the minimum value reached locally in the star core, with little relevance to the overall evolution. We can safely conclude that ambipolar diffusion is irrelevant during the first Myr of a neutron star life, for normal matter, in the standard cooling scenario, and magnetic fields $B \leq 10^{14}$ G. If dUrca processes are activated, the timescales are reduced considerably. The minimum timescale of our numerical solutions can reach $t_{amb}^{min} \simeq 1$ kyr while the global quantities t_{amb} and t_B reach values as low as 10 kyr, comparable to the expected ages of young X-ray pulsars. The imprint of fast neutrino cooling processes could be, in principle, visible as a fast magnetic field evolution in the core, driven by ambipolar diffusion. However, we need to incorporate superfluid/superconducting effects to be closer to the real case, which is done in the next section.

5.1 Superconductivity

When the star is superconducting or superfluid the ambipolar diffusion timescales may be very different than the normal matter case. Glampedakis et al. (2011b) derived analytical estimates for the solenoidal and non-solenoidal motion, which are given by

$$t^{sol} \sim \frac{4\pi m_p^* n_c L^2 \mathcal{R}_{np}}{H_{c1} B \tau_{pn}}, \quad t^{nsol} \sim \frac{4\pi n_c^2}{\lambda \mathcal{R}_{sf} H_{c1} B}, \quad (37)$$

where we have replaced m_p with an effective proton mass m_p^* . These timescales are determined by assuming that the particle scattering is dominant over the mutual friction dissipation (interaction between vortices and fluxtubes), which is approximately correct when $T_8 \gtrsim 3$.

In Fig. 10, we show the results for a superconducting/superfluid neutron star with mUrca reactions and a

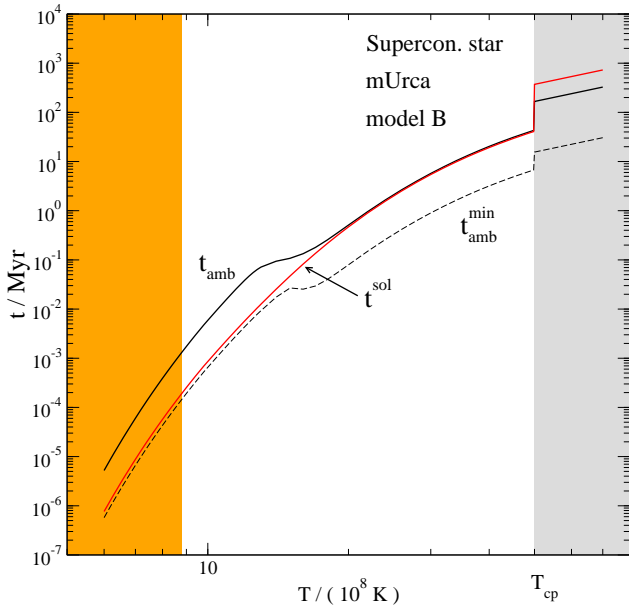


Figure 10. Variation of the ambipolar diffusion timescale with the temperature. Differently from the case shown in Fig.9, the star is superconducting. The β -reactions are driven by the mUrca process. The proton critical temperatures are $T_{cp} = 5 \times 10^9$ K and $T_{cn} = 10^9$ K. The black-solid line denotes the t_{amb} timescale, while the back-dashed line its minimum t_{amb}^{min} . The red-solid line refers to the volume average of the analytical solenoidal timescale t^{sol} (Eq. 37). The grey region denotes the temperature in which the star is not superconducting.

mixed magnetic field (model B). The proton critical temperature is $T_{cp} = 5 \times 10^9$ K, while the neutron transition to superfluidity is at $T_{cn} = 10^9$ K. After the superconducting transition the numerical timescale t_{amb} closely follows the analytical estimate t^{sol} . The bump associated with the transition to solenoidal flow is now smaller than in the non-superconducting case. The effect of the \mathcal{R}_{np} correction factor on the collision times results in a temperature dependence somewhat different from the T^2 scaling observed in the normal matter case.

Finally, we explore the effects of different proton critical temperatures in both mUrca and dUrca scenarios. The results are summarized in Fig. 11, where we show the timescales for $T_{cp} = 1, 2, 3, 4, 5 \times 10^9$ K for $T_{cn} = 10^9$ K (solid lines) and without neutron superfluidity (dot-dashed lines). The results show the little effect of the superfluid neutron transition, provided that the protons become superconducting at higher temperature. Minor differences are only visible when the two critical temperatures are similar $T_{cn} \simeq T_{cp}$. As expected, the temperature at which the transition to a solenoidal flow occurs, depends on the critical temperature T_{cp} and gradually increases for higher T_{cp} . The main result in the superconducting case is that, due to the weaker particle interactions, the global evolution timescales are sensibly reduced, being as short as 1-10 kyr for the mUrca case, or even of the order of years for the dUrca case. Our results show that when the critical temperature T_{cp} is higher, ambipolar diffusion can have a more significant impact on the magnetic field evolution. We must note again that in the dUrca case, cooling of the star also proceeds much faster,

and a more detailed study is needed before reaching more robust conclusions. But there is a potentially large effect of the proton superconducting gap on the core magnetic field evolution, which can be used to constrain its value through the combination of detailed modelling and astrophysical observations.

6 CONCLUSIONS

We have revisited the problem of ambipolar diffusion in neutron stars with axisymmetric magnetic fields, with special attention to the relevance of microphysical details (fast versus slow neutrino processes, normal versus superfluid matter). For a given magnetic field configuration and temperature, we determine numerically the local deviations from β -equilibrium and the relative velocity of the charged component (protons and electrons) with respect to the neutral component (neutrons), which causes the diffusion of the magnetic field.

In the wide range of temperatures and parameters explored, we could follow the variation of the velocity field and identify the temperature interval in which a solenoidal pattern becomes dominant in the flow. This transition to a solenoidal solution is due to the effect of the small departure from chemical equilibrium, which results in local pressure gradients that balance the irrotational part of the “magnetic force” acting on charged particles. The temperature at which this transition occurs depends on the β -reaction rates, superfluid/superconducting gap models, etc.

Typical core temperatures of neutron stars are between 10^8 K and 10^9 K, depending on the age and efficiency of neutrino reactions. Ambipolar diffusion can influence the evolution of the core magnetic field if, in this temperature interval, its timescale is of the order of the star age (from 10^3 to 10^6 yr). We find that such relatively short timescales can be achieved at low temperatures, after the transition to a solenoidal flow. However, in all cases dominated by an irrotational flow, ambipolar diffusion is expected to have little effect, as the magnetic field evolves on longer timescales.

For stars composed of normal matter with β -reactions controlled by the mUrca processes, the shortest evolution timescale is about 1 Myr at $T \approx 10^8$ K, for a mixed magnetic field configuration with $B_p = 10^{14}$ G at the magnetic pole and a maximum toroidal field of 10^{15} G. If the dUrca process is activated, shorter ambipolar diffusion timescales of the order of 10 kyr are reached at $T = 1 - 3 \times 10^7$ K. This could be the case of more massive NSs, where the central density is higher and additional neutrino channels could be opened.

However, NS cores are expected to be superfluid and superconducting and the suppression of both particle collisions and weak interaction rates substantially changes the results. In superfluid/superconducting cores, we find that, at about $T \approx 10^9$ K, the ambipolar drift timescale is about 1 kyr for mUrca processes and can be as short as about few years in stars with dUrca processes. The temperature at which the ambipolar flow reaches these timescales depends on the critical temperatures of superconducting and superfluid transitions. Our results show that ambipolar diffusion can play a key role in the magnetic field evolution in the superconducting core of a neutron star. However, there are uncertain aspects of the physical processes in this conditions

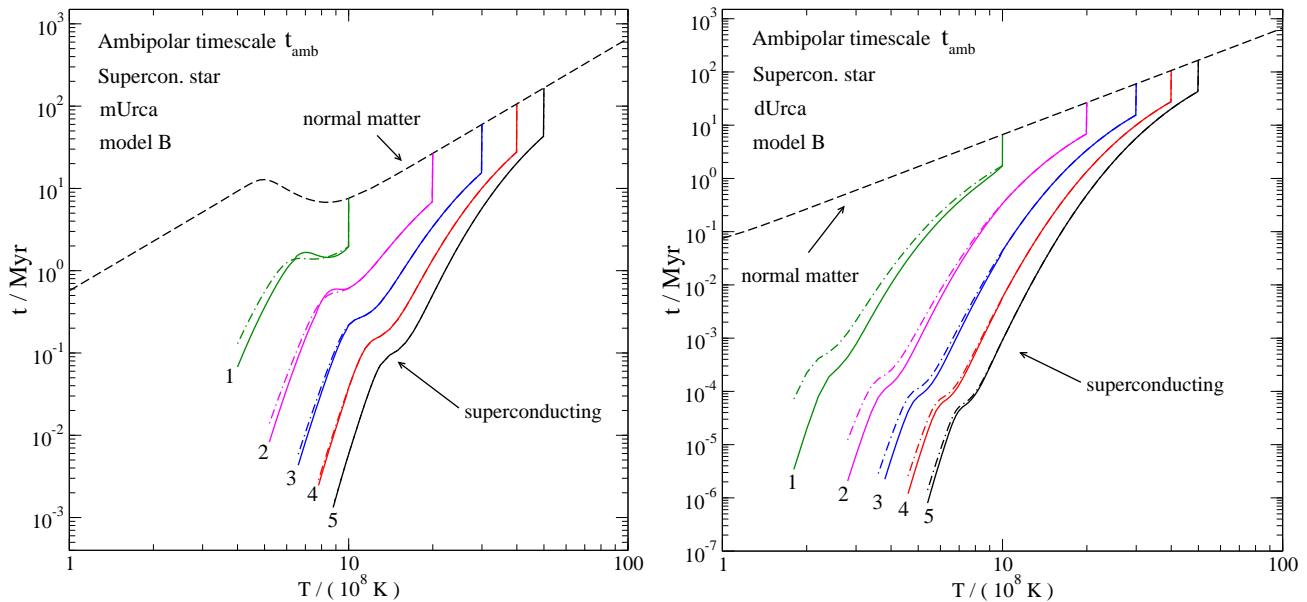


Figure 11. Ambipolar diffusion timescale t_{amb} as a function of temperature for superconducting models with different critical temperature T_{cp} , and with mixed-magnetic field (model B). The left- and right-hand panels show, respectively, the results for stars with mUrca and dUrca reactions. The dashed-line denotes the t_{amb} of a normal matter star, the colored-solid lines describes the t_{amb} for superconducting stars with $T_{cn} = 10^9$ K, while the dot-dashed lines refer to a model with normal neutrons. The number at the end of the superconducting t_{amb} denotes to the proton critical temperature, namely $T_{cp} = 1, 2, 3, 4, 5 \times 10^9$ K.

that need to be carefully revised, in particular the interactions between particles and fluxoids. The most interesting cases are when dUrca reactions are present, but in this situation the star also cools much faster, so it is unclear whether a substantial modification of the magnetic field configuration has observable consequences.

We need to go beyond the present approach that only gives information about snapshots of the NS life, at a fixed temperature and magnetic field configuration, and incorporate ambipolar diffusion consistently in magneto-thermal simulations. It is also possible that the non-linear evolution of the magnetic field brings the system quickly into a nearly force-free configuration, that reduces the impact of ambipolar diffusion. To firmly establish the role of the ambipolar diffusion in the evolution of neutron stars we must rely on multidimensional numerical simulations. The code developed in this work for calculating the global velocity field serves to set up the stage for this next step.

ACKNOWLEDGEMENTS

We would like to thank Andreas Reisenegger for his useful comments. A.P. acknowledges support from the European Union under the Marie Skłodowska Curie Actions Individual Fellowship, grant agreement n° 656370. This work is supported in part by the Spanish MINECO grants AYA2013-42184-P and AYA2015-66899-C2-2-P, and by the New Compstar COST action MP1304.

REFERENCES

Akgün T., Miralles J. A., Pons J. A., Cerdá-Durán P., 2016, arXiv:1605.02253

- Akgün T., Reisenegger A., Mastrano A., Marchant P., 2013, MNRAS, 433, 2445
Akgün T., Wasserman I., 2008, MNRAS, 383, 1551
Chandrasekhar S., 1961, Hydrodynamic and hydromagnetic stability. Oxford, Clarendon Press
Elfritz J. G., Pons J. A., Rea N., Glampedakis K., Viganò D., 2016, MNRAS, 456, 4461
Glampedakis K., Andersson N., Samuelsson L., 2011a, MNRAS, 410, 805
Glampedakis K., Jones D. I., Samuelsson L., 2011b, MNRAS, 413, 2021
Goldreich P., Reisenegger A., 1992, ApJ, 395, 250
Gourgouliatos K. N., Cumming A., 2014, MNRAS, 438, 1618
Gourgouliatos K. N., Cumming A., 2015, MNRAS, 446, 1121
Gourgouliatos K. N., Cumming A., Reisenegger A., Armaza C., Lyutikov M., Valdivia J. A., 2013, MNRAS, 434, 2480
Gourgouliatos K. N., Kondić T., Lyutikov M., Hollerbach R., 2015, MNRAS, 453, L93
Graber V., Andersson N., Glampedakis K., Lander S. K., 2015, MNRAS, 453, 671
Haensel P., Levenfish K. P., Yakovlev D. G., 2000, A&A, 357, 1157
Haensel P., Levenfish K. P., Yakovlev D. G., 2001, A&A, 372, 130
Haensel P., Schaeffer R., 1992, Phys. Rev. D, 45, 4708
Henriksson K. T., Wasserman I., 2013, MNRAS, 431, 2986
Hollerbach R., Rüdiger G., 2002, MNRAS, 337, 216
Hollerbach R., Rüdiger G., 2004, MNRAS, 347, 1273
Hoyos J., Reisenegger A., Valdivia J. A., 2008, A&A, 487, 789
Hoyos J. H., Reisenegger A., Valdivia J. A., 2010, MNRAS,

- 408, 1730
 Kondić T., Rüdiger G., Hollerbach R., 2011, *A&A*, 535, L2
 Lander S. K., 2013, *Phys. Rev. Lett.*, 110, 071101
 Lander S. K., 2014, *MNRAS*, 437, 424
 Lattimer J. M., Prakash M., Pethick C. J., Haensel P., 1991, *Phys. Rev. Lett.*, 66, 2701
 Levenfish K. P., Yakovlev D. G., 1994, *Astron. Lett.*, 20, 43
 Marchant P., Reisenegger, A., Valdivia, J., Hoyos, J. H., 2014, *ApJ*, 796, 94
 Mereghetti S., 2008, *A&ARv*, 15, 225
 Mereghetti S., Pons J. A., Melatos A., 2015, *Space Sci. Rev.*, 191, 315
 Pons J. A., Geppert U., 2007, *A&A*, 470, 303
 Pons J. A., Miralles J. A., Geppert U., 2009, *A&A*, 496, 207
 Reisenegger, A., Benguria, R., Prieto, J. P., Araya, P. A., Lai, D., 2007, *A&A*, 472, 233
 Roberts P. H., 1981, *Q. J. Mech. Appl. Math.*, XXXIV, 327
 Sawyer R. F., 1989, *Phys. Rev. D*, 39, 3804
 Shalybkov D. A., Urpin V. A., 1995, *MNRAS*, 273, 643
 Tinkham M., 2004, *Introduction to superconductivity*, 2nd edn.. Dover Publications, New York
 Turolla R., Zane S., Watts A. L., 2015, *Reps. on Progr. in Phys.*, 78, 116901
 Viganò D., Pons J. A., Miralles J. A., 2012, *Comp. Phys. Communications.*, 183, 2042
 Viganò D., Rea N., Pons J. A., Perna R., Aguilera D. N., Miralles J. A., 2013, *MNRAS*, 434, 123
 Wood T. S., Hollerbach R., 2015, *Phys. Rev. Lett.*, 114, 191101
 Yakovlev D. G., Levenfish K. P., 1995, *A&A*, 297, 717
 Yakovlev D. G., Shalybkov D. A., 1990, *Soviet Ast. Lett.*, 16, 86

APPENDIX A: THE EQUATION FOR $\Delta\mu$

In this section, we present the derivation of equation (14) and describe the approximation we have used. Taking the divergence of Eq. (9) and using the continuity Eqs. (11), we obtain

$$\nabla^2(\Delta\mu) - \frac{1}{b} \frac{\partial \Delta\mu}{\partial r} - \frac{x_n}{a^2 \lambda} \nabla \cdot (n_b \mathbf{v}_n) = \nabla \cdot \left(\frac{\mathbf{f}_{mag}}{n_c} \right) - \frac{1}{b} \frac{f_{mag}^r}{n_c}, \quad (\text{A1})$$

where we have assumed that the microphysical coefficients only depend on the radial coordinate, and we have defined

$$\frac{1}{a^2} = \frac{\lambda m_p^*}{x_n^2 n_c \tau_{pn}}, \quad \frac{1}{b} = \frac{d}{dr} \ln \left(\frac{m_p^*}{x_n n_c \tau_{pn}} \right). \quad (\text{A2})$$

Both a and b have dimensions of length.

To determine an equation for only $\Delta\mu$, we must remove the neutron velocity, which requires some further approximations. For instance, Goldreich & Reisenegger (1992) neglected the proton contribution to the total mass (i.e. $n_n = n_b$, $x_n = 1$), which leads to

$$\nabla \cdot (n_b \mathbf{v}_n) \approx \nabla \cdot (n_n \mathbf{v}_n) = \lambda \Delta\mu, \quad (\text{A3})$$

and thus

$$\nabla^2(\Delta\mu) - \frac{1}{b} \frac{\partial \Delta\mu}{\partial r} - \frac{1}{a^2} \Delta\mu = \nabla \cdot \left(\frac{\mathbf{f}_{mag}}{n_c} \right) - \frac{1}{b} \frac{f_{mag}^r}{n_c}, \quad (\text{A4})$$

where a and b are given by equation (A2) with $x_n = 1$.

In a slightly more rigorous way, we can write

$$\begin{aligned} x_n \nabla \cdot (n_b \mathbf{v}_n) &= x_n \nabla \cdot (n_n \mathbf{v}_n / x_n) \\ &= \lambda \Delta\mu - n_b \mathbf{v}_n \cdot \nabla(x_n), \end{aligned} \quad (\text{A5})$$

and assume that the last term can be neglected. This happens when x_n is constant throughout the star or when we are in the neutron reference frame where $\mathbf{v}_n = 0$. With this approximation, we obtain again Eq. (A4), but with the quantities a and b defined by equation (A2) with $x_n \neq 1$.

Alternatively, we can write equation (A5) as follows

$$x_n \nabla \cdot (n_b \mathbf{v}_n) = \lambda \Delta\mu - (n_b \mathbf{v}_b - n_p \mathbf{v}_p) \cdot \nabla(x_n), \quad (\text{A6})$$

and work in the coordinate system locally comoving with the baryons, where $n_b \mathbf{v}_b = n_n \mathbf{v}_n + n_p \mathbf{v}_p = 0$. Neglecting \mathbf{v}_b in equation (A6), we can determine again equation Eq. (A4), where the coefficient a is given by equation (A2) while the coefficient b has an extra factor x_n , i.e. it now reads

$$\frac{1}{b} \rightarrow \frac{d}{dr} \ln \left(\frac{m_p^*}{x_n^2 n_c \tau_{pn}} \right). \quad (\text{A7})$$

In any case, the difference between these various approximations (necessary to completely remove velocity terms from the equation) are always of the order of $1 - x_n \approx 0.1$.

APPENDIX B: TESTS

In this section we derive an analytical solution of equation (14) in order to test our numerical code and to understand the main properties of the solutions. The $\nabla \Delta\mu$ term becomes important at low temperature ($\approx 10^8$ K), when the weak interactions are sufficiently slow. This limit corresponds to the $L/a \ll 1$ case, which leads to the following simplified version of equation (14):

$$\nabla^2 \Psi + \frac{1}{b} \partial_r \Psi = \nabla \cdot \mathbf{F} + \frac{F^r}{b}, \quad (\text{B1})$$

where Ψ is a function of r and θ , \mathbf{F} a general vector field, and b is a coefficient that in this section we consider constant. Analytical solutions can be found for specific forms of the vector field \mathbf{F} .

In a bounded domain, with appropriate boundary conditions, we can use the Helmholtz-Hodge decomposition to decompose \mathbf{F} in its irrotational and solenoidal parts as follows

$$\mathbf{F} = \nabla \Phi + \nabla \times \mathbf{A}, \quad (\text{B2})$$

where $\Phi(r, \theta)$ is a scalar function and $\mathbf{A}(r, \theta)$ is a vector field. We consider the following expressions for the irrotational and solenoidal parts:

$$\Phi = r^2 (r - R_a)^2 P_2, \quad (\text{B3})$$

$$\mathbf{A} = r^2 (r - R_a)^2 \frac{dP_2}{d\theta} \hat{\phi}, \quad (\text{B4})$$

where R_a is a constant and $P_2 = (3 \cos^2 \theta - 1)/2$ is the $l = 2$ Legendre polynomial.

With this choice for \mathbf{F} , equation (B1) can be decomposed in spherical harmonics and becomes an ordinary differential equation in the radial coordinate. For a vector field $\mathbf{F} = c_{irr} \nabla \Phi + c_{sol} \mathbf{F}_{sol}$, where c_{irr} and c_{sol} are

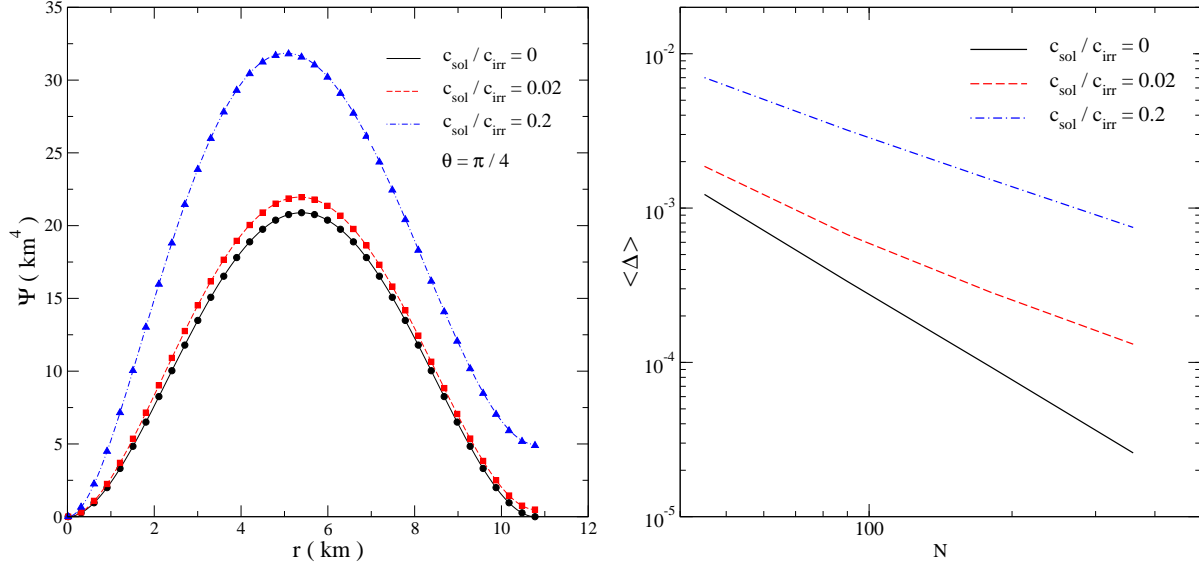


Figure B1. Left-hand panel: radial profile (at $\theta = \pi/4$) of the numerical and analytical solution of equation (B1) for three cases with $c_{sol} = 0$ (black-solid line), $c_{sol}/c_{irr} = 0.02$ (red-dashed line), and $c_{sol}/c_{irr} = 0.2$ (blue-dashed-dotted line). The numerical solution is represented by lines, while the analytical solution is denoted with symbols. Right-hand panel: log-log plot of the averaged error $\langle \Delta \rangle$ for various grid resolutions. In the horizontal axis, N is the number of points of a 2D grid with size $N \times N$.

two constants, we can derive an analytical solution $\Psi_{an} = \psi_{an}(r)P_2(\theta)$. The radial part of the solution, $\psi_{an}(r)$, which is regular at the origin ($r = 0$) is given by

$$\begin{aligned} \psi_{an}(r) = & \left[\left(4 + \frac{r}{b}\right) 6e^{-r/b} - 24 + \frac{18r}{b} - \frac{6r^2}{b^2} + \frac{r^3}{b^3} \right] \frac{c_0}{r^3} \\ & - \frac{3}{2} \left[2R_a^2 - \frac{8}{3}R_ar + r^2 - \frac{14}{3} \left(-\frac{12}{7}R_a + r \right) b \right. \\ & \left. + 14b^2 \right] r^2 c_{sol} + r^2 (r - R_a)^2 c_{irr}. \end{aligned} \quad (\text{B5})$$

The constant c_0 can be determined by imposing the external boundary condition at $r = R_a$. As described in Sec. 4, we consider the outer boundary condition $\partial_r \Psi = F^r(r = R_a) = 0$, which leads to the following expression:

$$c_0 = \frac{1}{2} \frac{R_a^5 (-7R_a + 8R_a + 14b) b^3 e^{(R_a/b)} c_{sol}}{(12b^2 + R_a^2) [-1 + e^{(R_a/b)}] - 6bR_a [1 + e^{(R_a/b)}]}. \quad (\text{B6})$$

We set $R_a = 10.788$ km, $b = 1$ km, $c_{irr} = 5 \times 10^{-2}$, and vary the amplitude of the ratio c_{sol}/c_{irr} . More specifically, we consider a purely irrotational vector field, i.e. $c_{sol} = 0$, and two cases with increasing solenoidal amplitude, respectively, $c_{sol}/c_{irr} = 0.02$ and $c_{sol}/c_{irr} = 0.2$. In the left panel of Fig. B1 we show the radial profile of the analytical solutions (lines) for $\theta = \pi/4$ compared to the numerical solutions (symbols). By increasing the solenoidal part of \mathbf{F} the solution changes significantly. This is an effect of a non-zero coefficient b . Note that in a realistic model the discontinuity of $\Delta\mu$ at the crust/core interface will be balanced by the elastic response of the crust. To study more in detail the accuracy of our numerical code we average the error of the relevant quantity, $\nabla\Psi$, in the grid. First, we evaluate the error in each point by

$$\Delta \equiv \frac{|\nabla\Psi - \nabla\Psi_{an}|}{\max|\nabla\Psi_{an}|} \quad (\text{B7})$$

and secondly we average the result in all the grid. Note that

in equation (B7) we have used the maximum as there are points where $|\nabla\Psi_{an}|$ vanishes. The variation of the averaged error $\langle \Delta \rangle$ with the grid resolution is shown in the right panel of Fig. B1 for the three cases with increasing solenoidal component (see legend). For the resolution used in this work, 360×360 points, the averaged error is less than 0.03% for the purely irrotational case, and increases with the presence of the solenoidal part to 0.1% when $c_{sol}/c_{irr} = 0.2$.